

Heterogeneous & Homogeneous & Bio- & Nano-

CHEM **CAT** CHEM

CATALYSIS

Accepted Article

Title: Unique Half Embedded/Exposed PdFeCu/C Interfacial Nanoalloy as High-Performance Electrocatalyst for Oxygen Reduction Reaction

Authors: Biraj Jyoti Borah, Himadri Saikia, Chiranjita Goswami, Kumar Kashyap Hazarika, Yusuke Yamada, and Pankaj Bharali

This manuscript has been accepted after peer review and appears as an Accepted Article online prior to editing, proofing, and formal publication of the final Version of Record (VoR). This work is currently citable by using the Digital Object Identifier (DOI) given below. The VoR will be published online in Early View as soon as possible and may be different to this Accepted Article as a result of editing. Readers should obtain the VoR from the journal website shown below when it is published to ensure accuracy of information. The authors are responsible for the content of this Accepted Article.

To be cited as: *ChemCatChem* 10.1002/cctc.201900469

Link to VoR: <http://dx.doi.org/10.1002/cctc.201900469>

Unique Half Embedded/Exposed PdFeCu/C Interfacial Nanoalloy as High-Performance Electrocatalyst for Oxygen Reduction Reaction

Biraj Jyoti Borah,^a Himadri Saikia,^a Chiranjita Goswami,^a Kumar Kashyap Hazarika,^a Yusuke Yamada,^b and Pankaj Bharali^{a*}

Abstract: Design of high-performance non-Pt electrocatalyst for fuel cell applications is greatly anticipated. Herein, we have developed a unique half-embedded and half exposed interfacial PdFeCu nanoalloy anchored onto carbon matrix. The stable electronic coupling between the carbon matrix and PdFeCu nanoalloy possess very fast interfacial electron transfer which in turn enhances the electron conductivity. This makes the trimetallic nanoalloy high performing oxygen reduction reaction (ORR) electrocatalyst in both basic and acidic media. The PdFeCu/C nanoalloy exhibits enhanced electrochemically active surface area than various PdFe/C bimetallics as well as benchmark 20 wt% Pt/C and Pd/C. As a result, it offers larger active sites for ORR and eased the electron transport during the electrocatalysis. It exhibits 1.5 and 2.4 fold higher mass activity in comparison to the Pt/C and Pd/C. Furthermore it exhibits long term stability and low onset potential compared to those of the other catalysts. Thus, the present investigation shows potential strategy for the design and synthesis of Pt-free electrocatalyst with remarkable catalytic activity and stability.

Introduction

The low physical and chemical stability of nanoparticles (NPs) mainly restrict the practical application of electrocatalysts (ECs) for fuel cell. Throughout the fuel cell operating conditions, NPs are often easily oxidized, dissolved in electrolyte, or separate from the support and agglomerated into larger particles, and thus losing their electrochemical catalytic performance during cycling.^[1] Therefore, numerous efforts have attempted to address the hurdles. These include modification of NPs with protective layer by carbon and/or modified carbon shells,^[2] inorganic oxide^[3] and graphitic material^[4,5] etc. Eventually the coated NPs exhibit improved electrocatalytic activity and long term durability compared to the uncoated one. Unfortunately, it was assessed that the protective layer can also decrease the activity by blocking the active sites of the EC.^[6] For instance, Guo et al.^[7a] reported embedded Pt nanocrystals into N-doped

carbon on carbon nanotube (Pt@CN_x/CNT), where the carbon layer effectively prevents the Pt NPs from migration, dissolution, detachment and aggregation during durability test and heat treatment at 900 °C. In another report, PtFe NPs with a very thin “dual purpose” N-doped carbon shell has been effectively synthesized.^[6] The carbon layer advantageously prevents PtFe NPs from agglomeration during the thermal annealing at ~700 °C. Even at this condition, the layer was still permeable for the reactant molecule and the catalytic activity of the NPs was not affected. Although, the processes exhibit good electrocatalytic activity, they have serious operating limitations. Time-consuming synthetic procedure, use of surfactants and very high pyrolysis temperature (700-900°C) effectively limits the electrocatalysts for practical application. Thus, the engineering of highly stable and efficient strategy for the realization of active fuel cell EC is still desirable. In particular, fuel cell ECs for cathodic oxygen reduction reaction (ORR) need to be very effective for overall performance of fuel cells.^[7b-e] This is because of the slow kinetics associated with the ORR process which limits active fuel cell materialization. In addition to this, the ORR activity of noble metals and their compounds are greatly influenced by lattice strain, electronic effect and surface defects.^[8a,b] The lattice strain plays an important role in the ORR of noble metal electrocatalysts, whereas the compressive lattice strain changes the d-band center of the metal catalysts which weakens the surface oxygen adsorption property of the catalyst surface.^[9] From the electronic effect, the alteration of the d band center for Pt or Pd through the formation of alloys with second metal could increase the kinetics of the ORR.^[10a,b] On the other hand abundant surface defect on NPs also alter the electrocatalytic performance by providing the accessible active sites for the reactant molecules.^[8]

Inspired by various strategies to improve ORR performance, we herein report the design of unique half embedded and half exposed PdFeCu nanoalloy on carbon matrix with multiple surface defects at relatively low temperature as presented in Scheme 1. The half embedded portion in carbon matrix effectively prevents the PdFeCu NPs from detachment, migration, dissolution, and aggregation during ORR process. The half exposed part, i.e. without protective carbon layer, become highly active as the reactant molecules (O₂ diffusion layer) could directly interact with these sites.^[8a] To the best of our knowledge, there is no report on the synthesis of half embedded and half exposed PdFeCu nanoalloys with lattice strain, and abundant surface defects for ORR in both acidic and alkaline electrolytes. It exhibits 1.5 and 2.4 fold higher mass activity in comparison to the Pt/C and Pd/C. Furthermore it shows long term stability and low onset potential compared to those of the Pd/C, Pt/C and other compositions of PdFe/C. Thus,

[a] B.J. Borah, Dr. H. Saikia, C. Goswami, K.K. Hazarika, Dr. P. Bharali
Department of Chemical Sciences, Tezpur University, Tezpur,
Assam-784 028, India
E-mail: pankajb@tezu.ernet.in

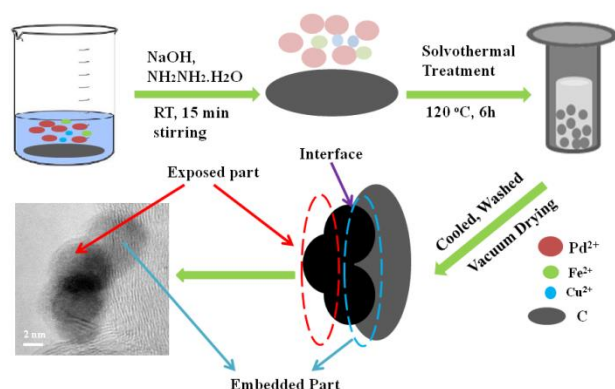
[b] Prof. Y. Yamada
Department of Applied Chemistry & Bioengineering, Graduate
School of Engineering, Osaka City University, 3-3-138 Sugimoto,
Sumiyoshi-ku, Osaka 558-8585, Japan

Supporting information for this article is given via a link at the end of the document.

this present strategy provides an efficient route for the synthesis of unique structured PdFeCu/C nanoalloy by altering d-band centre with rich surface defects and lattice strain.

Results and Discussion

The compositions of as prepared nanocatalysts are determined by EDS and ICP-OES analyses. The EDS analysis of Pd₃Fe_{0.5}Cu_{0.5}/C shows that only Pd, Fe, Cu and C are present in the EDS pattern with ~22 wt% loading of metals on carbon matrix. The corresponding EDS elemental maps show that homogeneous dispersion of metals on the carbon (Figure S1, Supporting information).



Scheme 1. Synthesis of unique half embedded and half exposed PdFeCu nanoalloy on carbon matrix.

The Pd, Fe and Cu atomic ratio are ca. 74.81%, 14.56% and 10.61%, which corroborate well with ICP-OES analyses. The loading of the metal obtained by TGA analysis is ~22% in the case of the Pd₃Fe_{0.5}Cu_{0.5}/C (Figure S2, Supporting information). It displays a sudden weight loss of the sample at about ~350 °C which is due to the oxidation of carbon to carbon dioxide in the sufficient oxidative environment. The residue obtained after burning of all the carbonaceous materials gives information about the loading of the total metal content. The powder XRD patterns of Pd₃Fe_{0.5}Cu_{0.5}/C, Pd₃Fe/C, PdFe/C, and PdFe₃/C (Figure S3A, Supporting information) show mainly characteristic peaks of face centred cubic (*fcc*) crystalline Pd signifying multiphase disordered structure. The diffraction peaks centred at ~40°, ~47°, and ~68° correspond to the (111), (200), and (220) reflections, respectively. These peaks are slightly shifted to higher angles relative to the pure Pd (JCPDS no. 87-0641) indicating the formation of an alloyed nanostructure.^[11] A broad peak observed at around ~25° is ascribed to the (002) reflection of a hexagonal structure in Vulcan XC-72R carbon. From Bragg's law^[12] the cell parameter (*a*) values of 0.3910 (PdFe₃/C), 0.3906 (PdFe/C), 0.39161 (Pd₃Fe/C) and 0.38918 nm (Pd₃Fe_{0.5}Cu_{0.5}/C) are calculated. The calculated '*d*' values of 0.2261 (Pd₃Fe/C) and 0.2246 nm (Pd₃Fe_{0.5}Cu_{0.5}/C) agrees well with the spacing between planes observed using HR-TEM (See Figure 1H). These values are rather smaller than those for bulk

Pd (JCPDS no. 87-0641, *a* = 0.3961 nm, *d* = 0.228 nm) and larger than bulk Fe (JCPDS no. 88-2324, *a* = 0.343 nm, *d* = 0.198 nm), and bulk Cu (JCPDS no. 85-1326, *a* = 0.361 nm, *d* = 0.208 nm) indicating the formation of PdFe bimetallic and PdFeCu trimetallic alloys. The relatively smaller values of '*a*' and '*d*' for Pd₃Fe_{0.5}Cu_{0.5}/C, as compared to the other PdFe alloys also implies effective lattice contraction. The Figure S3B (Supporting information) shows the N₂ adsorption-desorption isotherm of Pd₃Fe_{0.5}Cu_{0.5}/C which exhibits a high BET specific surface area of 69.8 m²/g and a large pore volume of 0.104 cc/g.

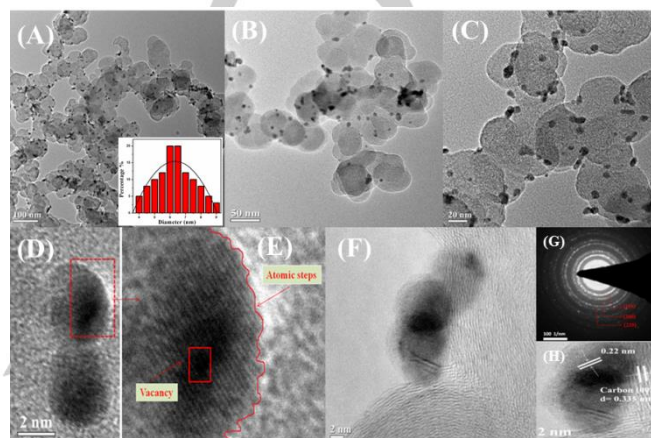


Figure 1. Typical (A) low, (B,C) medium, and (D-F,H) high resolution-TEM images of Pd₃Fe_{0.5}Cu_{0.5}/C, (G) corresponding SAED pattern, (E) is magnified HR-TEM image taken from (D), marked by the rectangle.

The shape and microstructure of Pd₃Fe_{0.5}Cu_{0.5}/C NPs are further studied by TEM and HR-TEM and presented in Figure 1. From the TEM images (Figure 1A-C) it could be observed that many nearly-spherical Pd₃FeCu NPs of dark contrast are highly dispersed on the larger particles of Vulcan XC72R carbon of lighter contrast. The average particle-size of Pd₃Fe_{0.5}Cu_{0.5} NPs is estimated to be about ~6-7 nm (inset in Figure 1A). The NPs exhibit various crystal defects on their surfaces, for instance vacancy, dislocation and low-coordinate atomic steps, as manifested in HR-TEM images (Figure 1D,E). Because of these coordinative unsaturation the NPs can serve as catalytic sites, successfully enhancing the electrocatalytic activity.^[14a] Furthermore, as shown in Figure 1F, Pd₃FeCu NPs are half embedded in the carbon matrix which generate rich interface that favors high electrocatalytic activity. The concentric circles with well-defined crystalline facets in the SAED pattern (Figure 1G) infer high crystallinity of the Pd₃FeCu/C NPs. The comprehensible *d*-spacings ~0.22 nm (Figure 1H) can be observed in the lattice fringes of a Pd₃FeCu/C NPs, close to the *fcc* Pd (111) facets, signifying high crystallization. The detailed morphological characterization of Pd₃Fe/C is also performed by TEM and HR-TEM analyses and presented in Figure S4 (Supporting information). As estimated, the Pd₃Fe/C alloy shows an analogous morphology and surface/interface structure with that of Pd₃Fe_{0.5}Cu_{0.5}/C NPs. Based on the above discussion, we could deduce that spherical and nearly homogeneous Pd-based NPs can be effectively synthesized by simple solvothermal

method without using any harmful structure directing solvents and surfactants. XPS is extensively performed to elucidate the chemical composition of NPs. Figure 2A-D illustrates the XP spectra of C 1s, Pd 3d, Fe 2p and Cu 2p regions of Pd₃Fe_{0.5}Cu_{0.5}/C. The C 1s core-level XP spectrum (Figure 2A) of Pd₃Fe_{0.5}Cu_{0.5}/C is slightly asymmetric and hence, can be deconvoluted into three different peaks *viz.*, a prominent peak at 284.6 eV along with two small peaks at 285.9 and 289.8 eV, consistent to form –C=C–, –C–O–, and O=C–O– bonds, respectively.^[14b,c]

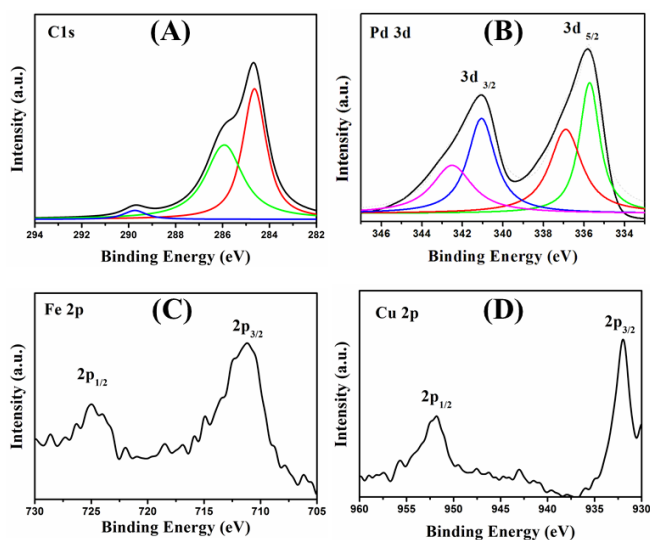


Figure 2. (A) C 1s, (B) Pd 3d, (C) Fe 2p, and (D) Cu 2p XP spectra of Pd₃Fe_{0.5}Cu_{0.5}/C.

The Pd 3d XP spectrum as presented in Figure 2B displays a doublet signal with binding energies of 335.7 and 341.0 eV for Pd 3d_{5/2} and Pd 3d_{3/2}, respectively, corresponding to the Pd signal. Additionally, small doublets observed around 336.9 and 342.5 eV could be indexed to the Pd 3d_{5/2} and Pd 3d_{3/2} peaks of PdO.^[15] Figure 2C shows the Fe 2p core-level spectrum for the NP. Two prominent peaks at 711.1 and 724.9 eV corresponds to the Fe 2p_{3/2} and Fe 2p_{1/2} core-level energies of iron oxide. The binding energy positions clearly indicates that the iron oxide in the NP is in the form of magnetite (Fe₃O₄).^[16] The emerging photoelectron peaks of Fe³⁺ may be attributed to the easy oxidation of zero valent iron (ZVI) in air, which could result in a layer of iron oxide around the ZVI NPs. The peaks observed at 932.0 and 951.8 eV from the Cu 2p_{3/2} and Cu 2p_{1/2} spin-orbit doublets, respectively, correspond to a metallic copper (Figure 2D), which is consistent with Cu NPs.^[17] The binding energy peaks of the three constituent elements Pd 3d_{5/2}, Fe 2p_{3/2} and Cu 2p_{3/2} are shifted as compared to that of the standard literature values. For Pd, a positive shift of ~0.50 eV, while, for Fe and Cu negative shifts of ~0.67 eV and ~0.50 eV, respectively, are observed in the binding energy values. The strong charge transfer between Pd, Fe and Cu is responsible for the alloy formation.^[18a] For the bimetallic Pd₃Fe/C, the clear shift of binding energy for both Pd and Fe peaks in comparison to the standard monometallic counterparts is a strong evidence of

efficient PdFe nanoalloy formation (See Figure S5 in the Supporting information). The electrocatalytic behavior of Pd₃Fe_{0.5}Cu_{0.5}/C and binary PdFe/C NPs modified glassy carbon electrode (GCE) are measured in N₂ and O₂ saturated 0.1 M KOH, as shown in Figure 3 and Figure S6-S8 in the Supporting information. As presented in the cyclic voltammogram (CV) in Figure 3A, a strong and well-defined reduction peak is observed in O₂-saturated 0.1 M KOH solution whereas no such feature is observed in N₂-saturated electrolyte. This signifies that Pd₃Fe_{0.5}Cu_{0.5}/C NP shows good ORR activity. To determine the kinetics of ORR, rotating disk electrode (RDE) measurement is performed in O₂ saturated 0.1 M KOH solution at a rotating rate of 400, 900, 1600, 2500 and 3600 rpm as shown in Figure 3B. Based on the ORR polarization curves, the number of electrons (n) transferred during ORR can be evaluated using the following Koutecky–Levich (K–L) equation.^[18b]

$$1/j = 1/j_k + 1/B \omega^{0.5}$$

$$B = 0.62 n F (D_{O_2})^{2/3} \nu^{-1/6} C_{O_2}$$

Where, *j* = current density, *j_k* = kinetic current density, *ω* = rotating rate of the electrode, *B* = value of slope obtained from the K–L plots, *F* = Faraday constant (96485 C mol⁻¹), *D_{O₂}* = diffusion coefficient of O₂ in 0.1 M KOH solution, *ν* = kinetic viscosity (0.01 cm² s⁻¹), *C_{O₂}* = bulk concentration of O₂ (1.2 × 10⁻⁶ mol cm⁻³), and *n* = the number of electrons transferred in the ORR process. The K–L (*j⁻¹* vs. *ω^{-1/2}*) plots obtained on the basis of the corresponding ORR polarization curves for Pd₃Fe_{0.5}Cu_{0.5}/C NP at a potential of –0.40, –0.50, –0.60, and –0.70 V show good linearity (Figure 3C) thereby implying a first-order kinetics for ORR. Figure 3D gives the corresponding plot of ‘n’ vs. potential (V). It can be seen that the ‘n’ values from –0.40 to –0.70 V are ~4.0, suggesting that the ORR mechanism on Pd₃Fe_{0.5}Cu_{0.5}/C NP follows the direct “4e⁻” pathway (O₂ + 2H₂O + 4e⁻ → 4OH⁻). The electrocatalytic ORR mechanism of binary PdFe/C NPs also follow the direct “4e⁻” pathway in the case of Pd₃Fe/C and PdFe/C NPs whereas “2e⁻” pathway possibly in the case of PdFe₃/C NPs (See Figure S6-S8 in the Supporting information).

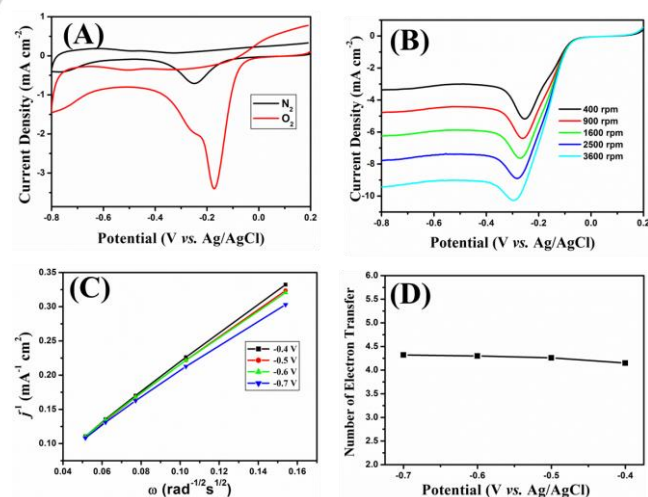


Figure 3. CV plots of Pd₃Fe_{0.5}Cu_{0.5}/C in N₂- and O₂-saturated 0.1 M KOH solution with a scan rate of 50 mV s⁻¹, (B) Rotating rate-dependent ORR polarization curves for respective NP with the scan rate of 10 mV s⁻¹, (C) K–L plots of *j⁻¹* vs. *ω^{-1/2}* at different potential obtained from (B), and (D) The plot of the number of transferred electrons vs. potential for Pd₃Fe_{0.5}Cu_{0.5}/C NPs.

To elucidate the electrocatalytic behavior of the NPs, the electrochemically active surface areas (ECSA) are calculated using CV curves in N_2 saturated 0.1 M KOH (Figure 4A). The peaks in the potential range $-0.5 - 0$ V originate from the palladium oxide reduction.^[18c] The calculated ECSA of $Pd_3Fe_{0.5}Cu_{0.5}/C$ ($63.22 \text{ m}^2\text{g}^{-1}$) is higher than Pd_3Fe/C ($32.99 \text{ m}^2\text{g}^{-1}$), $PdFe/C$ ($17.87 \text{ m}^2\text{g}^{-1}$), $PdFe_3/C$ ($8.3 \text{ m}^2\text{g}^{-1}$), standard Pt/C ($8.7 \text{ m}^2\text{g}^{-1}$), and standard Pd/C ($1.42 \text{ m}^2\text{g}^{-1}$). The higher ECSA values of the binary and ternary NPs can be attributed to the synergistic effect between the elements. Figure 4B shows the ORR polarization curves of $Pd_3Fe_{0.5}Cu_{0.5}/C$, $PdFe_3/C$, $PdFe/C$, Pd_3Fe/C , Pd/C, and Pt/C in O_2 -saturated 0.1 M KOH electrolyte at a rotation of 1600 rpm. The onset potential ($E_{\text{onset}} = 0.044$ V) and half-wave potential ($E_{1/2} = -0.145$ V) of $Pd_3Fe_{0.5}Cu_{0.5}/C$ NP are found to be more positive than those of standard Pd/C ($E_{\text{onset}} = -0.103$ V, $E_{1/2} = -0.212$ V), Pt/C ($E_{\text{onset}} = -0.069$ V, $E_{1/2} = -0.154$ V), $PdFe_3/C$ ($E_{\text{onset}} = -0.047$ V, $E_{1/2} = -0.168$ V), $PdFe/C$ ($E_{\text{onset}} = -0.036$ V, $E_{1/2} = -0.194$ V), and Pd_3Fe/C ($E_{\text{onset}} = -0.030$ V, $E_{1/2} = -0.147$ V) under identical conditions, suggesting superior ORR activity of the ternary $Pd_3Fe_{0.5}Cu_{0.5}/C$ NP. The overall ORR behavior follows the order: $Pd_3Fe_{0.5}Cu_{0.5}/C > Pd_3Fe/C > PdFe/C > PdFe_3/C > Pt/C > Pd/C$. Moreover, the apparent current density values follow the same order.

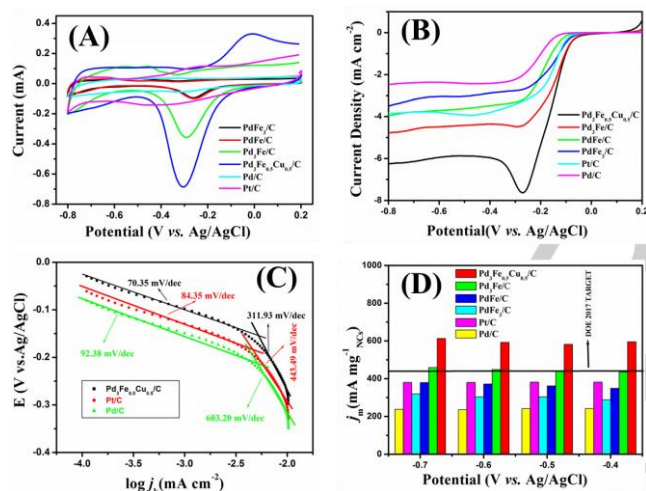


Figure 4 (A) CV plots of all the catalysts at N_2 -saturated 0.1 M KOH solution at a scan rate of 50 mV s^{-1} , (B) Comparison of rotating rate-dependent ORR polarization curves for different catalyst at 1600 rpm, (C) Tafel plots, and (D) Mass activities at 1600 rpm. (These values are calculated as per the loading mass of the NPs).

The Tafel plots derived from the ORR polarization curves for all NPs are presented in Figure 4C and Figure S9 (Supporting information). The Tafel slope calculated for $Pd_3Fe_{0.5}Cu_{0.5}/C$ in the high potential range (i.e., -3.9 V to -2.5 V) is $70.35 \text{ mV dec}^{-1}$, while the other in the low potential range is $311.93 \text{ mV dec}^{-1}$. The two Tafel slopes indicates different ORR behaviors in different potential ranges.^[19] These two slopes are comparatively smaller than those of Pt/C (84 and $443.4 \text{ mV dec}^{-1}$), Pd/C (92.38 and $603.2 \text{ mV dec}^{-1}$) as well as for other catalysts compositions and follows the order: Pd_3Fe/C (72 and $348.66 \text{ mV dec}^{-1}$) < $PdFe/C$ (74.59 and $373.17 \text{ mV dec}^{-1}$) < $PdFe_3/C$ (78.92 and

$393.74 \text{ mV dec}^{-1}$) < Pt/C (84 and $443.4 \text{ mV dec}^{-1}$) > Pd/C (92.38 and $603.2 \text{ mV dec}^{-1}$), in the high and low potential range, respectively. This indicates that $Pd_3Fe_{0.5}Cu_{0.5}/C$ has higher efficiency towards ORR as compared to that of the other catalyst systems studied and several reported Pd-based catalysts as detailed in Table S1 (Supporting information).

The mass activity (MA) and specific activity (SA) are the two important parameters for better assessment of the catalytic activity. The MA of various NPs under different potential at 1600 rpm are presented in Figure 4D. The MA and SA of $Pd_3Fe_{0.5}Cu_{0.5}/C$ at -0.4 V (595.8 mA mg^{-1} and 84 mA cm^{-2}) are much higher than Pt/C (382.2 mA mg^{-1} and 53.89 mA cm^{-2}) and Pd/C (241.6 mA mg^{-1} and 34.06 mA cm^{-2}) under the identical experimental conditions. The MA and SA values of $Pd_3Fe_{0.5}Cu_{0.5}/C$ are also larger than those of the $PdFe/C$ NPs which follows the order: Pd_3Fe/C (434.9 mA mg^{-1} and 61.32 mA cm^{-2}) > $PdFe/C$ (349 mA mg^{-1} and 49.20 mA cm^{-2}) > $PdFe_3/C$ (288.5 mA mg^{-1} and 40.67 mA cm^{-2}). These experimental findings are evident of the enriched kinetic ability of the $Pd_3Fe_{0.5}Cu_{0.5}/C$, making it an auspicious ORR electrocatalyst.

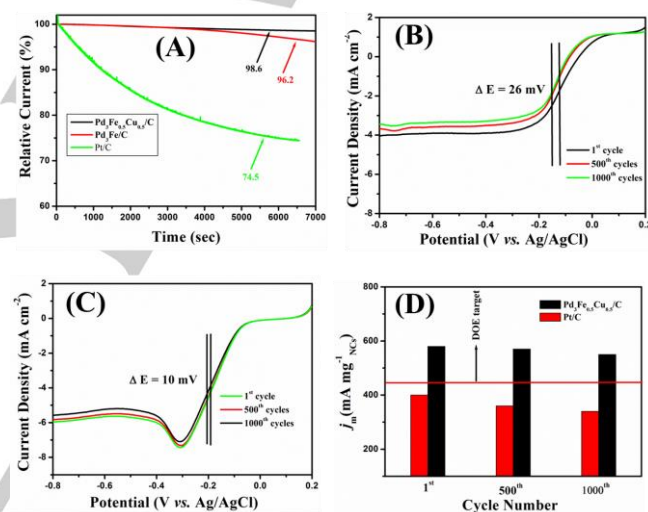


Figure 5. (A) CA curves of different electrocatalysts, recorded at -0.3 V in O_2 -saturated 0.1 M KOH solution with a rotation rate of 1600 rpm, ORR polarization curves of (B) Pt/C and (C) $Pd_3Fe_{0.5}Cu_{0.5}/C$ at 1600 rpm before and after the stability test at different potential scans, (D) Comparison of mass activity after the stability test at different potential scans at 1600 rpm.

The high durability of the electrocatalysts towards ORR is also an essential factor for energy conversion systems. Thus to check the durability, chronoamperometry (CA) test was performed in O_2 -saturated 0.1 M KOH at -0.3 V (vs. Ag/AgCl) with a rotation speed of 1600 rpm. It can be observed from Figure 5A that the initial activity decay for Pt/C and Pd_3Fe/C NP are $\sim 25.5\%$ and $\sim 3.8\%$, respectively after 7000 sec of testing, while the $Pd_3Fe_{0.5}Cu_{0.5}/C$ NP unveils only a loss of $\sim 1.4\%$ of its initial activity after 7000 sec, under identical experimental conditions. This demonstrates the excellent stability of the $Pd_3Fe_{0.5}Cu_{0.5}/C$ NPs. The structure and morphology of the $Pd_3Fe_{0.5}Cu_{0.5}/C$ NPs as measured by TEM analyses after the CA test are shown in Figure S10 (Supporting information). There is meager change in the morphology of the $Pd_3Fe_{0.5}Cu_{0.5}/C$ NPs after the CA test. To support the structural stability, an

accelerated durability test (ADT) is also performed for 1000 cycles for Pt/C and Pd₃Fe_{0.5}Cu_{0.5}/C NPs at 1600 rpm (Figure 5B,C). The MA of the Pd₃Fe_{0.5}Cu_{0.5}/C NPs has been deteriorated to a lower extent (5.17%) in comparison to Pt/C (11%) after 1000 potential CV cycles. There is a clear drop of onset potential in the case of Pt/C, whereas, the onset potential remains almost same after 500 and 1000 cycles for Pd₃Fe_{0.5}Cu_{0.5}/C. The E_{1/2} of Pt/C (26 mV) also shows a larger change compared to that of Pd₃Fe_{0.5}Cu_{0.5}/C (10 mV). Furthermore, methanol tolerance ability of Pd₃Fe_{0.5}Cu_{0.5}/C was performed by adding methanol (0.1 M) into the O₂-saturated 0.1 M KOH electrolyte in the CA test (Figure S11, Supporting information). After the addition of methanol (t = 150 s), a remarkable loss of current is observed in case of standard Pt/C signifying fast degradation of its electrocatalytic activity whereas there is no loss of activity in case of Pd₃Fe_{0.5}Cu_{0.5}/C up to 700 s. The above discussion indicates that Pd₃Fe_{0.5}Cu_{0.5}/C NP is the most efficient, stable and methanol tolerant electrocatalyst. To generalize the ORR behavior of the Pd₃Fe_{0.5}Cu_{0.5}/C NPs in the acidic electrolyte, we conducted electrocatalytic studies in 0.5 M H₂SO₄ solution. As presented in Figure S12 (Supporting information), it is apparent that Pd₃Fe_{0.5}Cu_{0.5}/C is very active towards ORR in 0.5 M H₂SO₄ solution as well. It can be seen that the 'n' values from 0.1 to 0.05 V are ~4.0, suggesting that the ORR mechanism on Pd₃Fe_{0.5}Cu_{0.5}/C NPs follows the direct "4e⁻" pathway (O₂ + 4H⁺ + 4e⁻ → 2 H₂O). To evaluate the durability, CA test was performed in O₂-saturated 0.5 M H₂SO₄ at 0.3 V (vs. Ag/AgCl) at 1600 rpm for Pd₃Fe_{0.5}Cu_{0.5}/C and Pt/C NPs. It is noticed from the Figure S13 (Supporting information) that the activity decay for Pd₃Fe_{0.5}Cu_{0.5}/C and Pt/C NPs are ~40% and ~70.5%, respectively after 7000 sec of testing. This shows that Pd₃Fe_{0.5}Cu_{0.5}/C is more stable even in acidic electrolyte over Pt/C NPs. However, the stability of NPs in acidic electrolyte is inferior in comparison to the basic electrolyte.

The enhanced ORR performance of Pd₃Fe_{0.5}Cu_{0.5}/C NPs is due to their unique structural and compositional superiorities. From the HR-TEM images, the unique half-embedded and half expose interface structure was seen. i.e., one-half of NPs are embedded into the carbon matrix and another part exposed from the carbon matrix. Therefore, there is a stable electronic coupling between the carbon matrix and Pd₃Fe_{0.5}Cu_{0.5} NPs. This means that the half embedded part possess very faster interfacial electron transfer ultimately enhancing the conductivity of the Pd₃Fe_{0.5}Cu_{0.5} NPs. Moreover the other exposed part is also highly active as the reactant molecule (O₂ diffusion layer) directly interacts with the catalyst layer. The carbon matrix also acts as superior support as they effectively prevent the NPs aggregation, improving the stability of the Pd₃Fe_{0.5}Cu_{0.5} in the electrochemical process. Furthermore, Pd₃Fe_{0.5}Cu_{0.5}/C nanoalloy exhibits many crystal defects on their surfaces, including vacancy, atomic steps and dislocation defects, that can work as abundant catalytically active sites accessible to the reactant, ultimately enhancing ORR activity. One of the salient parameters to understand the enhancement of ORR activity is the lattice strain effect in catalysts. The lattice strain changes the d-band center of the metal catalyst, which resolve the surface oxygen adsorption property on the catalyst surface.^[9,20] A down shift in the d-band center of Pd weakens the binding energy of absorption of intermediates such as OH⁻_{ads} and CO_{ads} thereby conserves more active sites on the catalyst surface. In this case,

we have calculated lattice strain from XRD data that Pd₃Fe_{0.5}Cu_{0.5}/C has the smallest lattice parameter among all compositions of PdFe/C, Pd/C and Pt/C. Moreover, the formation of alloy with the second metals can cause the alteration of d band center of Pd and Pt metal. For oxygen adsorption, an upshift of d-band centre can increase the interaction of the 2p states oxygen with the metal d states, i.e., forms a stronger metal-oxygen bond. On the other hand, a downshift of d-band causes a weak interaction with oxygen. The positive shifts of binding energy represent a downshift of d-band center with respect to Fermi level. The downshift of Pd d-band center can further be closely correlated with the weaker Pd-O bond energy, by means of which the intermediate OH_{ad} species adsorption on the Pd surface can be decreased,^[10,21] thus sustaining the more active sites for ORR and at the end resulting in the enrichment in ORR activity.^[10,22] The alteration of the d band center for Pt or Pd through the formation of alloys with second metals could increase the kinetics of the ORR. There are seminal theoretical reports of ORR where DFT has been used over various catalyst alloys with compositions of Pt₃X or Pd₃X (X = Cu, Ni, Co, Fe, Ag, Au, Ir, etc.) by using d-band center model.^[21,23] The upshift of ~0.50 and ~0.40 eV in the binding energies of Pd 3d_{5/2} for Pd₃Fe_{0.5}Cu_{0.5}/C and Pd₃Fe/C NPs in comparison to Pd/C as shown in Figure S14 (Supporting information) implies the aforesaid down shift trends of Pd d-band center which leads to the enhancement of the catalytic performance and acceleration in terms of mass activity of the ORR activity.

Conclusions

In summary, an efficient and long-term stable ORR electrocatalyst, Pd₃Fe_{0.5}Cu_{0.5}/C has been synthesized successfully. The modified lattice strain and d-band shift in Pd₃Fe_{0.5}Cu_{0.5}/C improves the catalytic efficiency relative to various compositions of PdFe/C. The unique half-embedded and half exposed interface structure of the nanoalloy offers stable electronic coupling between the carbon matrix and Pd₃Fe_{0.5}Cu_{0.5} NPs. As a result it impressively displays superior activity and stability towards ORR in comparison to commercial Pd/C and Pt/C electrocatalysts.

Experimental Section

Chemicals. The chemicals used are palladium(II) chloride (PdCl₂), copper(II) chloride dihydrate (CuCl₂·2H₂O), iron(II) chloride tetrahydrate (FeCl₂·4H₂O), sodium hydroxide (NaOH), hydrazine hydrate (NH₂NH₂·6H₂O), potassium hydroxide (KOH) etc. were purchased from Merck, India. Nafion, 20wt% Pt/C and 20wt% Pd/C were purchased from Alfa Aesar. Vulcan XC-72 R was obtained from Cabot Corporation in the form of research gift. All the chemicals were used as received and distilled water was used throughout the experiment.

Synthesis of Pd₃Fe_{0.5}Cu_{0.5}/C NPs. The 20wt% of Pd₃Fe_{0.5}Cu_{0.5}/C NPs was synthesized by the typical solvothermal method. To prepare the NPs, to a mixture solutions of 25 mL distilled water and 25 mL C₂H₅OH was mix, 0.197 mmol PdCl₂ (0.0350 g), 0.065 mmol FeCl₂·4H₂O (0.0132 g), 0.065 mmol CuCl₂·2H₂O (0.0112 g), and 0.1 g Vulcan XC-72 R were

added sequentially at room temperature with constant stirring. The mixture solution was ultra-sonicated for 5 min and 30 mL 0.05 M (0.2 g) NaOH solution was added dropwise at room temperature under constant stirring. After ca. 20 min, 2 mL 85% hydrazine hydrate was added dropwise to the mixture and stirred vigorously for another 25 min. The solution was then transferred into a Teflon cup (250 mL capacity) in a stainless steel autoclave. The autoclave was sealed and kept in an oven at 120 °C for 6 h and allowed to cool naturally (~2.5 h); the final product was washed several times with distilled water and then 50% C₂H₅OH to remove the unreacted NaOH and Cl⁻, and finally collected by centrifugation. The product was dried in a vacuum oven at 55 °C.

Synthesis of Pd_{4-x}Fe_x/C NPs. The synthesis procedures for Pd_{4-x}Fe_x/C NPs (x = 1, 2 and 3) were similar to that of Pd₃Fe_{0.5}Cu_{0.5}/C NPs keeping other conditions unaltered and only varying the initial mole ratio of Pd and Fe salt precursors to 1:3, 1:1 and 3:1.

Synthesis of Pd/C NPs. The Pd/C NPs were also synthesized using the method similar to that for Pd₃Fe_{0.5}Cu_{0.5}/C. In this case, only PdCl₂ was employed as the metal precursors.

Materials characterization. The X-ray diffraction (XRD) patterns of the samples were recorded on a Bruker AXS Model D8 focus instrument using nickel-filtered CuK α (0.15418 nm) radiation source at the 2 θ between 10° and 80°, the scan rate was 0.05° s⁻¹. The Inductively coupled plasma-optical emission spectrophotometry (ICP-OES) analysis was accomplished by using Perkin Elmer, USA instrument (Model: Optima 2100 DV) with the software Winlab-32. The loading of NPs on the carbon support was determined by Thermogravimetric analysis (Model TGA-50, Shimadzu). The flow rate of air atmosphere for the analysis was maintained at 30 mL min⁻¹ and heating rate at 10 °C min⁻¹ up to 700 °C. X-ray photoelectron spectroscopy (XPS) data were collected using a Shimadzu ESCA-3400 equipped with a Mg-anode X-ray gun (10 kV, 20 mA). Samples were Ar-etched for 60 s before the measurements. Accumulation times were 10-100 depending on signal intensity. The binding energies of the samples were charge-corrected with respect to the adventitious carbon (C 1s) peak at 284.6 eV. Transmission and high-resolution transmission electron microscopy (TEM and HR-TEM) investigations were performed on a FEI-Technai (G2 20 S-TWIN) instrument equipped with a slow-scan CCD camera and at an accelerating voltage of 200 kV. Energy-dispersive X-ray spectroscopy (EDS) elemental mapping were performed on an Oxford instrument attached to the "JEOL, JSM Model 6390 LV" scanning electron microscope operated at 15 kV. The Brunauer-Emmett-Teller (BET) surface areas were determined by N₂ physisorption using a Quantachrome Instruments (Model: NOVA1000e).

Electrocatalytic measurements. The catalytic activities of the freshly prepared Pd_{4-x}Fe_x/C NPs (x = 1, 2 and 3) and Pd₃Fe_{0.5}Cu_{0.5}/C catalysts for the electrocatalytic oxygen reduction were measured following a typical procedure. In brief, glassy carbon (GC) electrode (3 mm diameter, Rotating disk electrode, RDE) was polished with 0.005- μ m Al₂O₃ powder. A typical suspension of the carbon-supported catalysts was prepared by adding 5 mg of fresh catalyst to 0.5 mL 2-propanol, deionized water and 0.5% Nafion solution, respectively. The resultant mixture was sonicated for 30 min until it became a uniform dark ink. Then, 3 μ L of the suspension was quantitatively deposited onto the surface of the polished GC electrode. The electrode coated with a thin film of the ink was dried at 35°C under N₂ atmosphere for 6 h under vacuum. The modified GC electrode was inserted into an electrochemical cell and used as the working electrode. The cell includes two additional electrodes: a KCl saturated Ag/AgCl (Metrohm) as the reference electrode and a platinum wire (Metrohm) as the counter electrode. Cyclic voltammetry (CV) was performed using a computer-controlled electrochemical analyzer (Metrohm Autolab PGSTAT204 workstation, The Netherlands) at room temperature. The CV was measured in high purity N₂ and O₂ saturated

(0.1 M KOH and 0.5 M H₂SO₄) solution with scan rate 50 mV s⁻¹. RDE measurements were performed in O₂-saturated 0.1 M KOH. Oxygen was purged for at least 30 min before measurement and continuously bubbled through the electrolyte, in order to ensure the saturation of the electrolyte with O₂ and then blanketing the solution with an O₂ atmosphere during the entire experiment and all experiments were performed at room temperature. The electrochemical active surface area (ECSA) of the catalysts was evaluated by CVs in N₂-saturated 0.1 M KOH solution. For Pd-based catalysts, to evaluate the ECSA of the samples the columbic charge for the reduction of Pd-O monolayer, formed on Pd catalysts at the forward scan, was applied. The ECSA were calculated using the following equation: ECSA = Q/SL, where L is the Pd loading, Q is the collected charge that calculated from the Pd-O stripping, and S is a constant of 210 μ C cm⁻² that assumes a monolayer of Pd-O on the surface. The stability of the ORR electrode was tested using chronoamperometry. The chronoamperometric response for the ORR was obtained either at -0.3 V (vs. Ag/AgCl) in O₂-saturated 0.1 M KOH or 0.3 V (vs. Ag/AgCl) in O₂-saturated 0.5 M H₂SO₄ solution at 1600 rpm. CA response also performed to see the methanol tolerance ability at -0.3 V (vs. Ag/AgCl) in O₂-saturated 0.1 M KOH by using 0.1 M methanol. For comparison, a commercial 20 wt % Pd/C and Pt/C (Alfa Aesar) were measured under the identical experimental conditions.

Acknowledgements

The authors gratefully acknowledge the generous financial support from Science and Engineering Research Board (SERBDST No: SB/FT/CS-048/2014), New Delhi. SAIF, North-Eastern Hill University Shillong is acknowledged for TEM facilities.

Keywords: Nanoalloy, fuel cell, electrocatalysis, non-Pt electrocatalyst, oxygen reduction reaction.

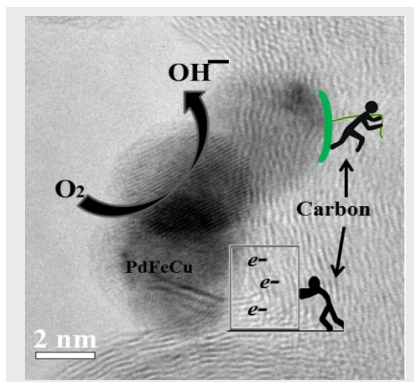
- [1] Y. Shao, G. Yin, Y. Gao, *J. Power Sources* **2007**, *171*, 558–566.
- [2] J. Deng, P. Ren, D. Deng, X. Bao, *Angew. Chemie Int. Ed.* **2015**, *54*, 2100–2104.
- [3] N. Cheng, M. N. Banis, J. Liu, A. Riese, X. Li, R. Li, S. Ye, S. Knights, X. Sun, *Adv. Mater.* **2015**, *27*, 277–281.
- [4] C. Baldizzone, S. Mezzavilla, H. W. P. Carvalho, J. C. Meier, A. K. Schuppert, M. Heggen, C. Galeano, J.-D. Grunwaldt, F. Schüth, K. J. J. Mayrhofer, *Angew. Chemie Int. Ed.* **2014**, *53*, 14250–14254.
- [5] Y. Hu, J. O. Jensen, W. Zhang, L. N. Cleemann, W. Xing, N. J. Bjerrum, Q. Li, *Angew. Chemie Int. Ed.* **2014**, *53*, 3675–3679.
- [6] D. Y. Chung, et al., *J. Am. Chem. Soc.* **2015**, *137*, 15478–15485. ("see Supporting Information")
- [7] a) L. Guo, W.-J. Jiang, Y. Zhang, J.-S. Hu, Z.-D. Wei, L.-J. Wan, *ACS Catal.* **2015**, *5*, 2903–2909; b) F. Liu, K. Sun, Z. Rui, J. Liu, T. Juan, R. Liu, J. Luo, Z. Wang, Y. Yao, L. Huang, P. Wang, Z. Zou, *ChemCatChem*, **2018**, *10*, 3049–3056; c) C. Goswami, K. K. Hazarika, P. Bharali, *Mater. Sci. Energy Technol.* **2018**, *1*, 117–128; d) K. K. Hazarika, C. Goswami, H. Saikia, B. J. Borah, P. Bharali, *Mol. Catal.* **2018**, *451*, 153–160; e) L. Zhang, X.-F. Zhang, X.-L. Chen, A.-J. Wang, D.-M. Han, Z.-G. Wang, J.-J. Feng, *J. Colloid Interface Sci.* **2019**, *536*, 556–562.
- [8] a) C. Li, Q. Yuan, B. Ni, T. He, S. Zhang, Y. Long, L. Gu, X. Wang, *Nat. Commun.* **2018**, *9*, 3702(1-9); b) A.-J. Wang, X.-F. Zhang, L.-Y. Jiang, L. Zhang, and J.-J. Feng, *ChemCatChem* **2018**, *10*, 3319–3326.
- [9] W. Xiao, M. A. Liutheviene Cordeiro, M. Gong, L. Han, J. Wang, C. Bian, J. Zhu, H. L. Xin, D. Wang, *J. Mater. Chem. A* **2017**, *5*, 9867–9872.
- [10] a) J. Greeley, I. E. L. Stephens, A. S. Bondarenko, T. P. Johansson, H. A. Hansen, T. F. Jaramillo, J. Rossmeisl, I. Chorkendorff, J. K. Nørskov, *Nat. Chem.* **2009**, *1*, 552–556; b) H.-Y. Chen, M.-X. Jin, L. Zhang, A.-J.

- Wang, J. Yuan, Q.-L. Zhang, J.-J. Feng, *J. Colloid Interface Sci.* **2019**, *543*, 1–8.
- [11] Y. Liu, S. Liu, Z. Che, S. Zhao, X. Sheng, M. Han, J. Bao, *J. Mater. Chem. A* **2016**, *4*, 16690–16697.
- [12] C. V. Boone, G. Maia, *Electrochim. Acta* **2017**, *247*, 19–29.
- [13] F. Wang, C. Li, L.-D. Sun, C.-H. Xu, J. Wang, J. C. Yu, C.-H. Yan, *Angew. Chemie Int. Ed.* **2012**, *51*, 4872–4876.
- [14] a) A.-X. Yin, X.-Q. Min, W. Zhu, H.-S. Wu, Y.-W. Zhang, C.-H. Yan, *Chem. Commun.* **2012**, *48*, 543–545; b) J. Du, C. Chen, F. Cheng J. Chen, *Inorg. Chem.*, **2015**, *54*, 5467–5474; c) Y. Lu, S. Zhao, R. Yang, D. Xu, J. Yang, Y. Lin, N.-E. Shi, Z. Dai, J. Bao, M. Han, *ACS Appl. Mater. Interfaces*, **2018**, *10*, 8155–8164.
- [15] J. Chai, F. Li, Y. Hu, Q. Zhang, D. Han, L. Niu, *J. Mater. Chem.* **2011**, *21*, 17922–17929.
- [16] T. Yamashita, P. Hayes, *Appl. Surf. Sci.* **2008**, *254*, 2441–2449.
- [17] F. Li, J. Li, X. Lin, X. Li, Y. Fang, L. Jiao, X. An, Y. Fu, J. Jin, R. Li, *J. Power Sources* **2015**, *300*, 301–308.
- [18] a) A. Ghosh, P. Chandran, S. Ramaprabhu, *Appl. Energy* **2017**, *208*, 37–48; b) K. Parvez, S. Yang, Y. Hernandez, A. Winter, A. Turchanin, X. Feng and K. Müllen, *ACS Nano*, **2012**, *6*, 9541–9550; c) F. Dehghani Sanij, H. Gharibi, *Colloids Surfaces A Physicochem. Eng. Asp.*, **2018**, *538*, 429–442.
- [19] Q. Shi, C. Zhu, C. Bi, H. Xia, M. H. Engelhard, D. Du, Y. Lin, *J. Mater. Chem. A* **2017**, *5*, 23952–23959.
- [20] L. A. Kibler, A. M. El-Aziz, R. Hoyer, D. M. Kolb, *Angew. Chemie Int. Ed.* **2005**, *44*, 2080–2084.
- [21] M. Shao, P. Liu, J. Zhang, R.R. Adzic, *J. Phys. Chem. B* **2007**, *111*, 6772–6775.
- [22] C. Koenigsmann, A. C. Santulli, K. Gong, M. B. Vukmirovic, W. Zhou, E. Sutter, S. S. Wong, R. R. Adzic, *J. Am. Chem. Soc.* **2011**, *133*, 9783–9795.
- [23] J. Greeley, I. E. L. Stephens, A. S. Bondarenko, T. P. Johansson, H. A. Hansen, T. F. Jaramillo, J. Rossmeisl, I. Chorkendorff, J. K. Nørskov, *Nat. Chem.* **2009**, *1*, 552–556.

Entry for the Table of Contents

FULL PAPER

The rich interface between the embedded PdFeCu nanoparticles and the carbon layer markedly affects the electronic structure of PdFeCu nanoalloy and contributed to the improvement in the catalytic activity and stability of PdFeCu/C. As a result, the PdFeCu/C catalyst exhibited an excellent stability and activity for oxygen reduction reaction.



*Biraj Jyoti Borah, Himadri Saikia,
Chiranjita Goswami, Kumar Kashyap
Hazarika, Yusuke Yamada, and Pankaj
Bharali**

Page No. 1-6

**Unique Half Embedded/Exposed
PdFeCu/C Interfacial Nanoalloy as
High-Performance Electrocatalyst for
Oxygen Reduction Reaction**